Article | Open Access

Energy Materials

Tao et al. Energy Mater. 2026, 6, 600118 DOI:10.20517/energymater.2026.123

Synergistic dipole and pseudo-hydrogen bonding in phosphate electrolytes for stable elevated temperature lithium batteries

Chengcheng Tao[1], Zhiqiang Han[4], Yin Shen[1], Yike He[1], Yuting Wang[1], Gen Li[1], Bo Zhao[1], Mingshan Wang[1,2,3,*], Michael Zaiser[1,5,*], Xing Li[1,2,3,*]

Keywords:
Lithium metal batteries, tributyl phosphate, dipole/pseudo-hydrogen bond, high-temperature, safety

Citation: Tao, C.; Han, Z.; Shen, Y.; He, Y.; Wang, Y.; Li, G.; Zhao, B.; Wang, M.; Zaiser, M.; Li, X. Synergistic dipole and pseudo-hydrogen bonding in phosphate electrolytes for stable elevated temperature lithium batteries. *Energy Mater.* **2026**, *6*, 600118. https://dx.doi.org/10.20517/energymater.2026.123

Received: 14 May 2026
First Decision: 2 Jul 2026
Revised: 29 Jul 2026
Accepted: 14 Aug 2026
Published: 16 Sep 2026

Academic Editors: Yuping Wu, Jianguo Lu
Copy Editor: Fangling Lan
Production Editor: Fangling Lan

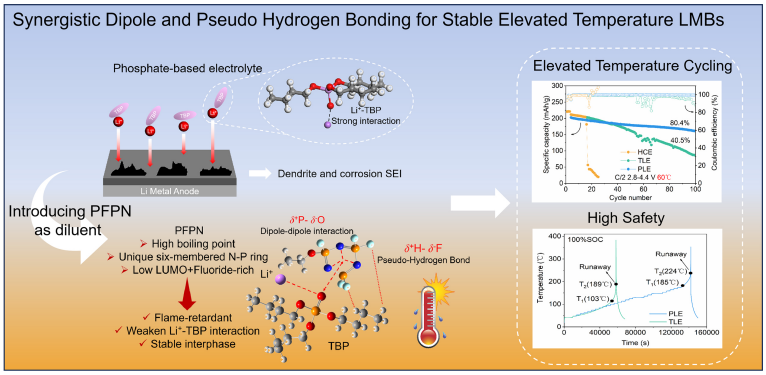

Abstract

Tributyl phosphate (TBP) is regarded as a potential solvent for elevated temperature lithium metal batteries due to its high boiling point, low vapor pressure and excellent thermal stability. However, the strong interaction between the polar P=O groups of phosphate and Li^+ slows down Li^+ kinetics, and the vigorous reductive decomposition of phosphate ester compounds on the anode leads to an unstable and fragile solid electrolyte interphase (SEI), resulting in poor cycling stability at elevated temperatures. Herein, an electrolyte system that employs functionalized ethoxylated (pentafluoro)cyclotriphosphazene (PFPN) and TBP establishes a dipole/pseudo-hydrogen bond synergistic solvation relationship to resolve the strong coordination between TBP and Li^+ and the resulting SEI instability. Specifically, the synergistic dipole-dipole interactions

[1]School of New Energy and Materials, Southwest Petroleum University, Chengdu 610500, Sichuan, China.
[2]SILK ROAD Research Center of Sustainable Energy Conversion and Utilization, Southwest Petroleum University, Chengdu 610500, Sichuan, China.
[3]Vanadium Flow Battery Engineering Research Center of Sichuan Province, Southwest Petroleum University, Chengdu 610500, Sichuan, China.
[4]Beijing Advanced Innovation Center for Materials Genome Engineering, Center for Green Innovation, School of Mathematics and Physics, University of Science and Technology Beijing, Beijing 100083, China.
[5]Department Werkstoffwissenschaften, Lehrstuhl für Werkstoffsimulation (WW8), FAU Erlangen-Nürnberg, Fürth 70962, Germany.

*Correspondence to: Dr. Mingshan Wang, Dr. Xing Li, School of New Energy and Materials, Southwest Petroleum University, Chengdu 610500, Sichuan, China; SILK ROAD Research Center of Sustainable Energy Conversion and Utilization, Southwest Petroleum University, Chengdu 610500, Sichuan, China; Vanadium Flow Battery Engineering Research Center of Sichuan Province, Southwest Petroleum University, Chengdu 610500, Sichuan, China. E-mail: wangmingshan@swpu.edu.cn; lixing@swpu.edu.cn; Dr. Michael Zaiser, School of

New Energy and Materials, Southwest Petroleum University, Chengdu 610500, Sichuan, China; Department Werkstoffwissenschaften, Lehrstuhl für Werkstoffsimulation (WW8), FAU Erlangen-Nürnberg, Dr. Mack Strasse 77, Fürth 70962, Germany. E-mail: michael.zaiser@fau.de

between the N-P ring (δ^+P) of PFPN and the P=O group (δ^-O) of TBP, combined with pseudo-hydrogen bonds between δ^-F of PFPN and δ^+H of TBP alkyl chains, generate a drag effect that weakens Li^+-TBP coordination, thereby enhancing Li^+ transport kinetics. Moreover, the low lowest unoccupied molecular orbital level of PFPN enables its preferential decomposition on the anode, which cooperates with the FSI^--rich inner solvation sheath to construct a robust =P-N/LiF-rich SEI and cathode electrolyte interphase (CEI), effectively suppressing side reactions between TBP and the Li metal anode. Consequently, the NCM811||Li cells using the electrolytes deliver outstanding rate capability and stable long-term cycling at 60 °C. In addition, the Ah-level Li||NCM811 pouch cell shows excellent safety, characterized by no ignition upon nail penetration at full charge and a high thermal runaway onset of 224 °C from accelerating rate calorimetry testing.

INTRODUCTION

In the pursuit of novel energy storage solutions that can withstand extreme environmental conditions, the safety concerns associated with lithium batteries in high-temperature environments and the lack of related fundamental research have emerged as significant technological impediments, necessitating prompt solutions[1-3]. The development of electrolyte systems that are suitable for operation in high-temperature environments is of significant importance. Current commercialized carbonate-based electrolyte systems exhibit several drawbacks when used in lithium batteries under extreme high-temperature conditions[4,5], including flammability, low vapor pressure, and poor thermal stability; difficulty in forming a stable cathode electrolyte interphase (CEI), leading to accelerated transition metal dissolution and rapid battery capacity/voltage decay; difficulty in forming a stable solid electrolyte interphase (SEI) at the anode, which causes lower Coulombic efficiency (CE), greater propensity for Li dendrite growth, and accumulation of inactive lithium and intensified electrode interface side reactions, severe current collector corrosion, and heightened risk of thermal runaway.

Phosphate esters are considered promising high-temperature flame-retardant solvents owing to their excellent flame retardancy, thermal stability, an appropriate electrochemical window, and high solubility for lithium salts[6]. However, due to their inherent difficulty in forming a stable SEI on Li metal anode (LMA) surfaces, they have traditionally been used primarily as flame-retardant additives[7]. As the carbon chain lengthens, phosphate esters exhibit increased boiling points and reduced vapor pressures, better meeting the demands of high-temperature environments for electrolytes[8,9]. However, the accompanying increase in molecular chain length and molecular weight leads to higher viscosity, resulting in poor compatibility with both positive and negative electrodes, low lithium-ion conductivity, and poor cycling stability[10-12]. Therefore, appropriate co-solvents or diluents are necessary to tailor the solvation structure and boost the high-temperature electrochemical performance.

Addressing these challenges calls for concerted actions, including the fine-tuning of Li^+-phosphate ester affinities and the development of innovative electrolytes, which together serve to elevate the electrochemical performance of rechargeable batteries. Weak-solvation electrolytes incorporating weakly coordinating solvents represent one such strategy and have been widely reported to reduce Li^+-solvent coordination, promote rapid Li^+ desolvation, and achieve high Li plating/stripping reversibility[13-16]. However, the low boiling points of such solvents hinder their application at high temperatures. In addition, various film-forming additives with strong solvation ability have been employed to tune the Li^+ solvation structure, where additives competitively coordinate with Li^+, thereby alleviating Li^+-solvent interactions[17-19]. Nevertheless, trace amounts of additives may pose challenges in maintaining the cycle performance of lithium metal

Table 1. Chemicals and materials

Chemicals and materials	Manufacturer
Lithium bis(fluorosulfonyl)imide (LiFSI)	Nippon Catalyst Corp
Tributyl phosphate (TBP)	Shenzhen Biyuan Electronics Corp
Ethoxy(pentafluoro)cyclotriphosphazene (PFPN)	Shanghai Aladdin Biochemical Technology Corp
2,2,3,3-Tetrafluoro-1-(1,1,2,2-tetrafluoroethoxy)propane (TTE)	Shanghai Aladdin Biochemical Technology Corp
Lithium iron phosphate (LFP)	Dongguan Keruder Experimental Equipment Corp
$LiNi_{0.8}Co_{0.1}Mn_{0.1}O_2$ (NCM811)	Dongguan Keruder Experimental Equipment Corp
50-μm-thick Li-Cu composite strips	China Energy Lithium Corp
Polyethylene diaphragm	Celgard Company (USA)

batteries (LMBs). In contrast, diluents are excluded from the inner solvation sheath and exhibit only weak interactions with the solvent components, offering an alternative approach to reduce the viscosity brought by long-chain phosphate ester electrolytes at high temperatures and to modulate Li^+-solvent interactions[20-22]. However, most diluents reported thus far are hydrofluoroethers (HFEs), such as 1,1,2,2-tetrafluoroethyl-2,2,3,3-tetrafluoropropyl ether (TTE). These compounds suffer from low boiling points (< 100 °C) and high volatility, restricting their operational temperature window. Furthermore, the low flash points of HFE diluents and their toxic decomposition products raise safety and environmental concerns. PFPN, a commercialized flame-retardant additive with a high boiling point of 125 °C, ensures enhanced cell safety. PFPN has been shown to simultaneously stabilize both the LMA and the high-voltage cathode in LMBs[23-25]. Based on these advantages, PFPN represents a superior alternative to HFEs and other diluents for high-temperature/high-voltage LMBs, offering intrinsic safety and a wide electrochemical window.

Herein, employing a solution of lithium bis(fluorosulfonyl)imide (LiFSI) in TBP as the solvent, along with PFPN as the functional diluent (we denote this system as PLE), we focus on elucidating a dipole/pseudo-hydrogen bond synergistic mechanism between solvents, investigate the effects of this unique intermolecular interaction on the Li^+ solvation structure, interfacial chemistry, and high-temperature cycling stability by combining theoretical calculations, molecular dynamics simulations, and multi-scale characterizations, and propose a universally applicable design strategy for flame-retardant phosphate electrolytes. Subsequently, the developed electrolyte achieves non-flammability, a broad electrochemical stability window (ESW) extending to 5.23 V, suppression of Li dendrite formation, construction of robust =P-N/LiF-rich SEI, and significantly boosts the cycle life of Li||NCM811 batteries at both 30 and 60 °C. Notably, the Ah-level Li||NCM811 pouch cell exhibits outstanding safety performance. It withstands nail penetration at 100% state of charge without ignition, and its thermal runaway temperature reaches as high as 224 °C as determined by accelerating rate calorimetry (ARC). For comparison, we tested two other electrolytes to reveal the role of dipole/pseudo-hydrogen bond in regulating solvent chemistry. The former is LiFSI:TBP (denoted as HCE), while the latter combines TBP as the main solvent with TTE as the diluent (denoted as TLE).

EXPERIMENTAL

Materials

All raw materials required for electrolyte preparation and cell assembly were sourced from commercial suppliers without extra purification treatment prior to use. The materials and their sources are compiled in Table 1.

Electrolytes

The electrolyte HCE was 3M LiFSI/TBP, TLE was LiFSI:TBP:TTE = 1:1.2:5 by molar composition, and PLE was LiFSI:TBP:PFPN = 1:1.2:5 by molar composition. All electrolyte formulations were prepared inside an

Table 2. Instruments used for experimental characterization and testing

Instrument	Manufacturer	Model	Country of origin
Scanning electron microscope (SEM)	Zeiss	Sigma 300	Germany
X-ray photoelectron spectrometer (XPS)	Thermo Fisher Scientific	ESCALAB 250Xi	USA
X-ray diffractometer (XRD)	Rigaku	SmartLab	Japan
Raman spectrometer	Horiba	LabRAM HR Evolution	France
Fourier-transform infrared spectrometer (FTIR)	Thermo Fisher Scientific	Nicolet iS50	USA
Nuclear magnetic resonance spectrometer (NMR)	Bruker	Avance III 400	Germany
Thermogravimetric analyzer (TGA)	Netzsch	STA 449 F3	Germany
Differential scanning calorimeter (DSC)	TA Instruments	Q2000	USA
Accelerating rate calorimeter (ARC)	THT	EV+	UK
Conductivity meter	Mettler Toledo	S230	Switzerland
Viscosity meter	Shanghai Jingke	JD-9S	China
Contact angle tester	Dataphysics	OCA25	Germany
Optical microscope	Leica	DM2500 M	Germany

argon-filled glove box, where the concentrations of water and oxygen were strictly maintained below 0.1 ppm.

Characterizations

Scanning electron microscopy (SEM) and transmission electron microscopy (TEM) were employed to examine the morphology of lithium deposits and cathode materials. Raman spectroscopy was performed in the range of 200-2,000 cm^{-1}, and TGA was carried out in air at a heating rate of 10 °C min^{-1}. X-ray photoelectron spectroscopy (XPS) was employed to analyze the surface compositions of both the lithium metal and the cathode. For electrolyte characterization, conductivity and viscosity were measured using a S230 conductivity meter and a JD-9S viscometer, respectively; each test was repeated three times and the results were averaged. Wettability was assessed via an OCA25 contact-angle goniometer. Flame-retardancy tests involved infiltrating 19-μm-thick PE separators with 150 μL of electrolyte, igniting them with an ignition gun inside a fume hood, and recording the combustion process on video. Finally, optical microscopy was employed for *in situ* observation of the lithium deposition morphology. The nail penetration test was performed on the Battery Crush Nail Penetration Tester (FL-86105, Dongguan Bowen Instrument Company) under ambient air conditions. The tested pouch cells had undergone 3 cycles at 0.05C between 3-4.3 V with 100% state of charge. A stainless-steel nail with a diameter of 10 mm was driven through the pouch cells at a speed of 5 mm s^{-1} and held for 10 s. A compilation of the experimental equipment used for characterization and testing is given in Table 2.

Batteries

Both coin cells and pouch cells were assembled. All coin cells used had CR2032 format. All test cells were assembled and hermetically sealed under compaction pressure ranging from 5 to 10 MPa. The amount of electrolyte used in the coin cell was 70 μL. The cathode and lithium electrode sheets had diameters of 12 and 16 mm, respectively. The active material loading of NCM811 and LFP was 9.2 and 12.3 mg cm^{-2}, respectively. With an electrolyte-to-capacity (E/C) ratio of 1.98 g Ah^{-1} and negative-to-positive (N/P) capacity ratio of 1.09, 1 Ah pouch cells assembled using NCM811 cathode (the active material loading is 26.48 mg cm^{-2}) and LMA (50 μm). The 1 Ah pouch cells prepared through this stacking process were composed of four lithium strips and three NCM811 electrode sheets in total.

Electrochemical tests

The ESW was characterized by linear sweep voltammetry (LSV), which was performed from 0 to 6 V at a sweep rate of 1 mV s^{-1}. Electrochemical impedance spectroscopy (EIS) spectra were acquired in the frequency range of 0.01-100 kHz using a 5 mV AC perturbation. For the Li||Cu half-cells, the CE was measured at 0.5 mA cm^{-2} with a fixed Li deposition capacity of 1 mAh cm^{-2}. To precisely quantify the *CE* of LMAs, the Aurbach protocol (modified) was utilized, as given in

$$CE = (Q_s + nQ_c)/(Q_T + nQ_c) \quad (1)$$

Under this testing protocol, a fixed quantity of charge denoted as Q_T is first applied to plate metallic lithium onto the copper substrate to construct a lithium reservoir. A fraction of the charge supply, marked Q_c, is subsequently utilized to drive lithium plating and stripping cycling between the working and counter electrodes for n repeated cycles. Upon the completion of n cycling rounds, the residual lithium stored within the reservoir is fully stripped until the preset cut-off voltage is reached. The total charge collected during this final stripping process is recorded as Q_s, which quantifies the amount of unreacted lithium retained after the cycling procedure.

The Li^+ transference number (t_{Li}^+) was evaluated by the Bruce-Vincent method via chronoamperometry (CA) on Li||Li cells at a polarization potential of 10 mV until steady-state conditions were established. Interfacial resistances before and after polarization were recorded using EIS.

The Tafel equation ($\eta = a + b\log(I)$) was employed to determine the exchange current density by fitting the measured current-potential data and extrapolating to $\eta = 0$, with the parameters a and b obtained from the fitting. Galvanostatic measurements of Li||Li symmetric cells were performed at 0.5 mA cm^{-2} and 1 mAh cm^{-2}. Constant-current cycling of coin cells was conducted with different voltage cutoffs: 2.5-4.2 V for Li||LFP and 2.8-4.4 V for Li||NCM811. Pouch cells were cycled between 3.0 and 4.3 V under various temperature conditions.

Computational details

Molecular geometries of LiFSI TBP TTE and PFPN underwent geometric optimization within density functional theory (DFT) calculations adopting the B3LYP functional paired with the 6-31g** basis set. IEFPCM implicit solvent model was integrated into every computational task to capture solvent-induced interactions. DFT-D3 dispersion correction was further incorporated to improve calculation accuracy. Gaussian 16 program suite supported the whole set of DFT computational tasks. Multiwfn and VMD software packages handled subsequent characterization covering highest occupied molecular orbital (HOMO)/lowest unoccupied molecular orbital (LUMO) and electrostatic potential electrostatic potential (ESP) related analyses.

For molecular dynamics (MD) simulation, three electrolyte systems were built to investigate the solvation structure of Li^+. In system I, the monomer ratio of LiFSI and TBP = 1:1.2 and 50 LiFSI, 60 TBP were randomly inserted into cubic box. In system II, the monomer ratio of LiFSI:TBP:TTE = 1:1.2:5 and 50 LiFSI, 60 TBP and 250 TTE were randomly inserted into a cubic box. In system III, the monomer ratio of LiFSI:TBP:PFPN = 1:1.2:5 and 50 LiFSI, 60 TBP and 250 PFPN. The molecules were inserted into a 10 × 10 × 10 nm^3 simulation box randomly. The acpepy script generated GAFF force field topology files for all involved molecules. Molecular dynamics simulations were run with the 2,019.3 release of the GROMACS software suite. Overall potential energy stems from multiple valence-related contributions such as bond stretching angle bending torsion and nonbonded atomic interactions. Lennard-Jones potential functions defined all nonbonded atomic contacts while standard geometric mean combination rules governed van der Waals

forces between distinct atomic types. For every simulated system, the calculation workflow began with energy minimization of starting atomic configurations through the steepest descent approach.

After this optimization stage, a 2.0 ns NPT ensemble MD simulation ran for preliminary system equilibration with a fixed 2 fs time step. The system temperature rose linearly from 0 to 298 K/333 K over 1,000 picoseconds and maintained the corresponding temperature value throughout the whole subsequent simulation period. 50 ns production molecular dynamics run followed the pre-equilibration step. The v-rescale thermostat algorithm maintained steady 298/333 K temperature across all simulation trajectories while the Parrinello-Rahman algorithm sustained atmospheric pressure at 1 atm. The LINCS algorithm restricted all atomic bond lengths and periodic boundary conditions were adopted for all simulation boxes. Short-range nonbonded atomic interactions were truncated at a distance of 1.2 nm and particle mesh Ewald methods handled calculations for long-range electrostatic effects. Simulation trajectories were recorded every 2 ps and visualized with the VMD 1.9.3 software package.

RESULTS AND DISCUSSION

Design strategy and solvation structures of the electrolytes

The regulation of electrolyte solvation structures is a critical scientific issue in optimizing electrode/interface electrochemical behavior at elevated temperatures, as it directly determines the chemical composition, structural characteristics, and interfacial dynamic stability of the SEI and the CEI. The spatial distribution and reactivity of anions, solvent molecules, and diluents at the electrode/electrolyte interface are fundamentally governed by the electrolyte solvation structure, which in turn dictates the pathways and products of interfacial reactions[26-28]. In PLE electrolyte, the incorporation of PFPN as a functional additive plays a pivotal role [Figure 1A]. The electron distribution within the molecular structure of its six-membered N-P ring exhibits δ^+P character, which leads to significant complementary dipole-dipole interactions with the δ^-O character of the strongly polar P=O group in tributyl phosphate (TBP). Concurrently, the electronegative δ^-F in PFPN and the partially positively charged δ^+H on the alkyl chains of TBP establish a pseudo-hydrogen bonding network. The synergistic effect of these two types of weak intermolecular interactions generates a unique drag force within the electrolyte, effectively weakening the coordination strength between lithium ions and TBP molecules. This interaction reduces the desolvation energy barrier for lithium ions, which enables a more uniform nucleation and deposition of lithium on the lithium metal anode surface, achieving a dendrite-free and compact deposition morphology. On the anode side, PFPN with a low LUMO energy level [Supplementary Figure 1] preferentially participates in reductive decomposition. It acts synergistically with the reduction process of FSI^- anions to construct an inorganic LiF-rich interphase layer, effectively enhancing interfacial stability to suppress both dendritic and parasitic reactions between TBP and LMA. On the cathode side, PFPN undergoes electrochemical decomposition under high-voltage oxidation conditions, generating nitrogen-phosphorus inorganic derivatives with high chemical stability. The decomposition products generate a dense, uniform, and highly ion-conductive CEI film *in situ* on the surface of the NCM811. The resulting interfacial layer effectively inhibits the dissolution of transition metal ions and subsequent structural degradation, while also mitigating the oxidative decomposition of the electrolyte at high voltages. Consequently, the lattice structural integrity and interfacial charge transfer kinetics of the NCM811 cathode material are preserved during prolonged cycling. Such dual-side interfacial engineering, driven by PFPN, delivers robust interfacial chemistry that sustains the stable performance of high-nickel ternary LMBs under thermal stress.

To elucidate the interaction mechanism between PFPN and TBP, we analyzed their charge distributions via ESP calculations [Figure 1B], which critically govern diluent-solvent interactions. Evidently, the O atom of the -P=O group in TBP concentrates nearly all negative charge, while positively charged P atoms are uniformly distributed along the phosphorus skeleton of PFPN. This facilitates electronic-attraction-driven

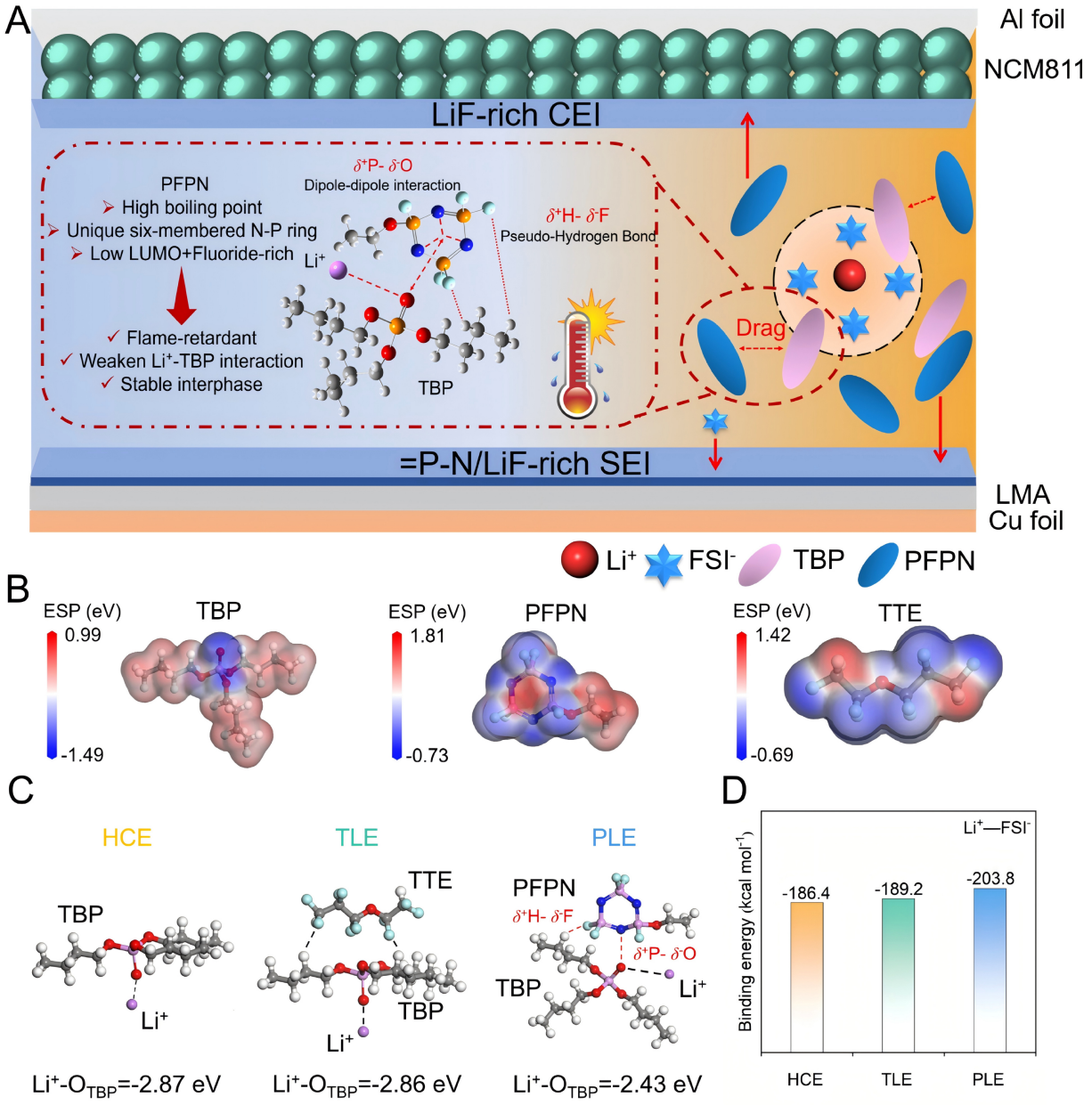

Figure 1. Design principle of electrolytes. (A) Schematics of the evolution of solvation structures at the cathode and anode interfaces in PLE electrolyte. (B) The optimized geometric configurations and electrostatic potential of TBP, PFPN and TTE. (C) Schematics of varied interactions and binding energies between Li^+ and TBP in HCE, TLE and PLE electrolytes. (D) The binding energy of Li^+-FSI^- in HCE, TLE and PLE electrolytes.

coordination between the two components. The binding energies between Li^+ and TBP were obtained from DFT calculations [Figure 1C]. In HCE electrolytes, the solvation structure is governed by Li^+-TBP interaction, with a Li^+-O_{TBP} binding energy of -2.87 eV. Introducing TTE as a diluent induces hydrogen bond-like interaction between C-F (δ^-F) in TTE and C-H (δ^+H) in TBP. While this reduces the Li^+-TBP binding energy, the P-O group in TBP maintains strong Li^+ coordination, demonstrating TTE's inability to disrupt core Li^+-TBP interaction. In contrast, in the PLE system, not only does the P-F (δ^-F) group in PFPN participate in hydrogen bond-like interactions, but the positively charged N-P ring also forms dipole-dipole attractions with the negatively charged P-O group in TBP. This dual interaction mechanism significantly weakens Li^+-TBP coordination and modifies the Li^+ solvation structure. The observed reduction in Li^+-O_{TBP}

binding energy to -2.43 eV further confirms the presence of dipole/pseudo-hydrogen bond interaction between PFPN and TBP. Concurrently, the binding energies of Li^+-FSI^- under different electrolytes were calculated using density functional theory. As demonstrated in Figure 1D, the binding energy (ΔE) of Li^+-FSI^- in PLE was calculated to be -203.8 kcal mol^{-1}, which exceeds the -186.4 and -189.2 kcal mol^{-1} of Li^+-FSI^- in HCE and TLE respectively, thereby confirming the increase of Li^+-FSI^- interactions due to the dipole/pseudo-hydrogen bond interaction between PFPN and TBP in the electrolyte.

Modulating solvent internal structures acts as a core factor to optimize the performance of high-temperature electrolyte systems. We investigated the microscopic solvation structures of various electrolytes through classical MD simulations. MD snapshots of HCE reveal a high proportion of free solvent molecules and salt anions, with minimal anion participation in the primary solvation sheath [Figure 2A]. In contrast, upon introducing TTE or PFPN as diluents, Li^+ coordinates with both TBP and FSI^- anions, while TTE/PFPN remains uncoordinated, freely surrounding but not directly bonding to Li^+ ions or FSI^- anions [Figure 2B and C]. Changes in the solvated structure of Li^+ are also manifest when the radial distribution functions (RDF) determined from the MD simulations are studied. In HCE and TLE [Figure 2D and E] electrolytes, the interaction between Li^+ and the oxygen atoms of TBP is significantly stronger than that with FSI^-, as evidenced by the closer proximity of the corresponding first coordination peaks in the RDF. In contrast, in the PLE electrolyte prepared by the addition of PFPN [Figure 2F], the initial peaks of Li-O_{TBP} and Li-O_{FSI^-} are shifted and the coordination number of FSI^- increases accordingly. Meanwhile, we conducted molecular dynamics simulations for the three electrolyte systems at 60 °C [Supplementary Figure 2]. The results demonstrated that even as the temperature increased, the solvation structural characteristics remained unchanged, which lends further support to the hypothesis that the synergy of dipole/pseudo-hydrogen bond interactions between the diluent and solvent in the PLE electrolyte allows for enhanced Li^+-FSI^- interactions. In addition, in the PLE, no discernible peaks were observed from 0 to 10 Å for the Li-O_{PFPN} and Li-N_{PFPN} RDF, indicating that PFPN is not directly coordinated to Li^+.

The solvation structure of PLE was systematically investigated using Raman spectroscopy, with the corresponding spectra presented in Figure 2G. The characteristic vibrational bands of FSI^- anions were subjected to spectral deconvolution, revealing distinct peaks at 742, 754, and 766 cm^{-1}, which are assigned to solvent-shared ion pairs (SSIP), contact ion pairs (CIP), and ionic agglomerates (AGG), respectively, consistent with previous literature[29]. In HCE, Li^+ cations are extensively coordinated with FSI^- anions, thereby establishing a solvation environment that thermodynamically favors the preferential decomposition of FSI^- over the organic solvent. Upon the introduction of TTE, a notable increase in the fraction of CIPs is observed, attributable to the emergence of weak pseudo-hydrogen bond interactions between TTE and the solvation species. In contrast, the PLE formulation exhibits a markedly higher proportion of AGGs, which is ascribed to the strong dipole-dipole and pseudo-hydrogen-bonding interactions between PFPN and TBP. These robust intermolecular interactions promote the participation of additional Li^+ in the solvation network, consequently facilitating the formation of a SEI enriched in inorganic components.

Complementary insights into the modulation of Li^+-solvent interactions are obtained via nuclear magnetic resonance (NMR) spectroscopy, wherein the ^7Li nucleus is particularly sensitive to the coordinating species present in the primary solvation shell. Variations in the local chemical environment induce changes in the electron density surrounding Li^+, which are directly reflected in the ^7Li NMR chemical shift. Among the three investigated electrolytes, the HCE displays the most upfield-shifted ^7Li resonance at -0.65 ppm [Figure 2H], indicative of the strongest electronic shielding effect around Li^+, which originates from the tight binding of FSI^- anions within the primary solvation sheath, which enhances electron donation to the Li^+ center. The subsequent addition of either TTE or PFPN to the HCE results in a downfield shift of the ^7Li peak, signifying reduced shielding and weakened Li^+-TBP interactions. Notably, the PLE electrolyte exhibits a more

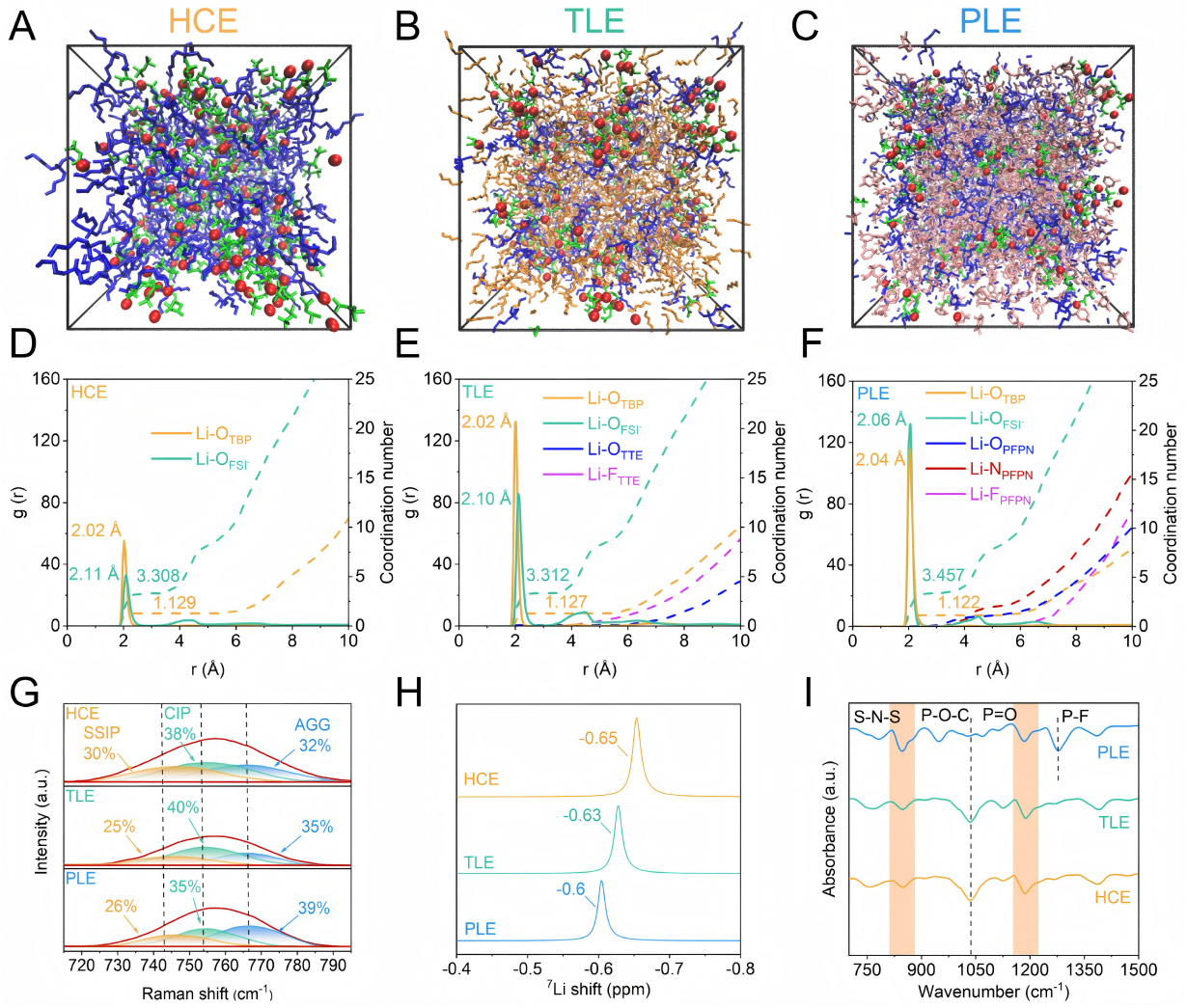

Figure 2. Solvation structure of electrolytes. MD simulation snapshots of (A) HCE, (B) TLE and (C) PLE. Radial distributions functions (RDF) and corresponding coordination of Li-O_{TBP}, Li-O_{FSI^-}, Li-O_{PFPN}, Li-N_{PFPN}, and Li-F_{PFPN} pairs calculated from MD simulation of (D) HCE, (E) TLE and (F) PLE. (G) Raman spectra of different electrolytes in the range of 720-790 cm^{-1}. The peaks near 742, 754, and 766 cm^{-1} are assigned to SSIP, CIP, and AGG. (H) ^{7}Li NMR spectra of various electrolytes. (I) FTIR spectra of HCE, TLE and PLE.

pronounced downfield shift (-0.60 ppm), which is attributed to the stronger "drag effect" arising from the synergistic dipole/pseudo-hydrogen-bond interactions between PFPN and TBP, effectively pulling electron density away from Li^+.

Further corroboration was provided by Fourier-transform infrared (FTIR) spectroscopy, which highlights the superiority of PFPN over conventional inert hydrogen fluoride ether diluents [Figure 2I]. The absorption band centered at approximately 840 cm^{-1} is assigned to the asymmetric S-N-S stretching mode of the FSI^- anion. The relative integrated intensity of this band increases in the order HCE < TLE < PLE, accompanied by a distinct red shift in the peak position. Collectively, the FTIR observations, in conjunction with MD simulations and NMR spectral data, strongly indicate that a greater number of FSI^- anions participate in the Li^+ solvation shell in the PLE system, thereby promoting the formation of anion-rich solvated clusters.

Physical and chemical properties of electrolytes

Flame retardation is a critical safety attribute for liquid electrolytes in LMBs. As illustrated in Figure 3A, systematic flammability tests demonstrate that both HCE and PLE exhibit superior fire resistance, confirming their non-flammable nature and inherent safety under abusive conditions. In contrast, TLE

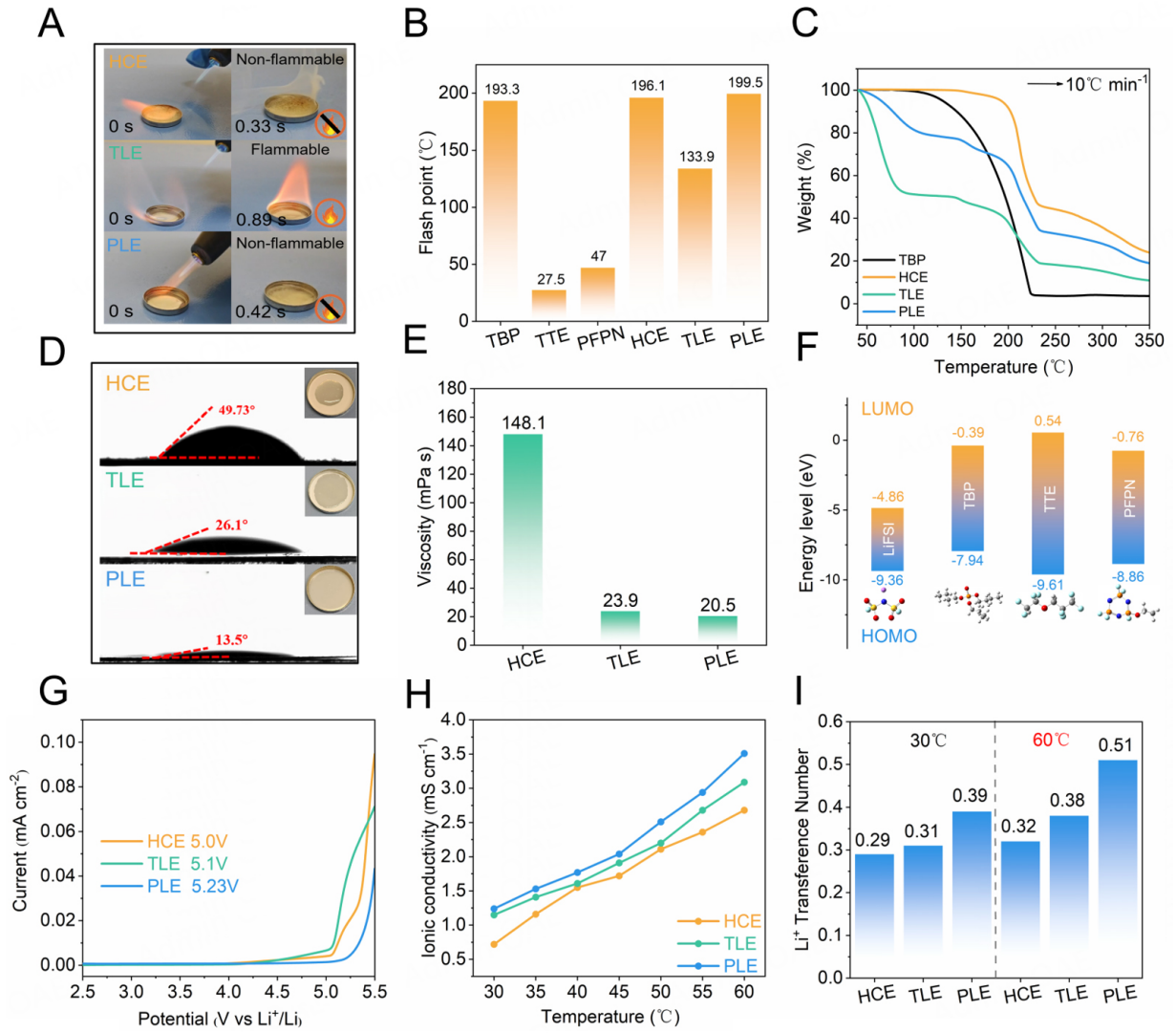

Figure 3. Physical and chemical properties of electrolytes (A) Evaluation of flame-retardant properties of HCE, TLE and PLE electrolytes. (B) Flash points of HCE, TLE and PLE electrolytes (averages over three measurements). (C) Thermogravimetric analysis (TGA) of HCE, TLE and PLE electrolytes. At 30 °C, (D) Wettability of HCE, TLE and PLE electrolytes and (E) viscosity of HCE, TLE and PLE electrolytes. (F) The calculated HOMO and LUMO energy level (eV) diagrams for lithium salts LiFSI and solvents TBP, TTE, PFPN. (G) Linear sweep voltammetry curves (LSV) of HCE, TLE and PLE electrolytes. (H) Conductivity of HCE, TLE and PLE electrolytes at different temperatures. (I) Li^+ transference numbers of HCE, TLE, and PLE at 30 and 60 °C.

remains readily combustible owing to its high proportion of volatile ether solvents. Complementary flash point measurements were conducted for HCE, TLE, and PLE [Figure 3B], with each reported value representing the average of three independent measurements. The results corroborate the flammability observations: all components of the PLE and HCE formulations are non-flammable and exhibit substantially elevated flash points. In marked contrast, TLE displays several intrinsic drawbacks, particularly under elevated temperature conditions, including pronounced flammability, a low flash point and posing significant safety risks.

The thermal stability of electrolytes under elevated temperature conditions is critical to the cycling durability and safety of LMBs. This property was systematically evaluated via thermogravimetric analysis (TGA). Benefiting from the high boiling point and low volatility of PFPN, the PLE electrolyte exhibits only 20% mass loss when heated to 100 °C, whereas the TLE counterpart loses approximately 50% of its initial mass under

identical thermal conditions [Figure 3C]. This pronounced disparity underscores the substantially superior thermal robustness of the PLE at elevated temperatures, which is advantageous for high-temperature battery operation. As depicted in Figure 3D and E, upon increasing the lithium salt concentration to 3 M, both the TLE and the PLE exhibit significantly lower viscosities compared to HCE, which suffers from high viscosity due to extensive ion aggregation. Notably, with the introduction of PFPN as a non-polar diluent, the viscosity of the PLE further diminishes to an exceptionally low value of 20.5 mPa·s. This drastic reduction is attributed to the effective disruption of large ionic aggregates and the weakening of Li^+-solvent/anion interactions. The markedly reduced viscosity substantially enhances the wetting capability of the PLE toward both the polyolefin separator and the electrode materials. Consequently, the contact angle of the PLE on a polyolefin separator is as low as 13.5°, which is much lower than those of HCE and TLE, indicating superior electrolyte spreading and interfacial contact.

According to frontier molecular orbital theory, molecules with a lower 415 LUMO energy tends to accept electrons more readily in reduction, whereas those with a higher HOMO energy are more susceptible to electron loss during oxidation[30,31]. DFT calculations [Figure 3F] reveal that the LUMO energy level of PFPN is -0.76 eV, which is considerably lower than that of TBP (-0.39 eV). This indicates that PFPN is more readily reduced than TBP, promoting the formation of fluoride-rich decomposition products. Subsequent reactions generate LiF/-P=N-containing species on the LMA, contributing to the overall interfacial reaction pathway. The resulting inorganic-rich SEI effectively suppresses lithium dendrite growth and robustly stabilizes the phosphate ester/LMA interface[32]. By contrast, TTE exhibits a relatively high LUMO energy level, rendering it incapable of preferential reduction; thus, TBP is reduced first on the LMA side. Consequently, TTE does not participate in SEI formation, leading to an SEI with a diminished LiF content. These theoretical predictions are further corroborated by LSV. The LSV curve of PLE displays a stable anodic current plateau extending up to 5.23 V [Figure 3G], demonstrating a wide ESW and confirming the feasibility of PLE for high-voltage LMB applications. This anodic stability surpasses that of HCE (5.0 V) and TLE (5.1 V). Furthermore, as shown in Figure 3H and I, Supplementary Figures 3-8, the PLE exhibits higher ionic conductivity and a superior Li^+ transference number compared to HCE and TLE. These enhancements underscore the critical role of PFPN in weakening Li^+-TBP interactions, facilitating greater incorporation of FSI^- anions into the primary solvation sheath, and thereby facilitating the desolvation of Li^+.

Analysis of the SEI evolution

Sustained structural damage and reconstruction of SEI films at elevated temperatures adversely affect cycling stability, making a compact and robust SEI highly desirable. The compatibility between PLE and LMAs was evaluated by measuring Li||Cu cells in a full plating/stripping cycle test [Figure 4A]. After the introduction of PFPN, the average CE of PLE increased to 97.6% in 200 cycles, demonstrating excellent compatibility with the LMA. For comparison, the average CE of the HCE over 50 cycles is only 91.9%, followed by a significant decrease in CE, indicating that the SEI in the HCE is not stable enough to withstand long-term cycling. TLE showed an average CE of 96.0% over 90 cycles. In the modified Aurbach measurements [Supplementary Figure 9], under the conditions of a current density of 0.5 mA cm^{-2} and an area capacity of 1 mAh cm^{-2}, due to the excellent Li^+ transfer kinetics, the average cycling CE of PLE reached 98.5% after 50 cycles, indicating an effective suppression of parasitic reactions. In contrast, the CE of HCE and TLE is only 97.3% and 95.7% respectively. In addition, the rate performance of Li||Cu cells in HCE, TLE and PLE was investigated. As shown in Supplementary Figure 10, when the current density increased from 0.5 to 4 mA cm^{-2}, internal short circuits occurred in the Li||Cu cells of HCE and TLE, indicating severe growth of lithium dendrites. In contrast, the polarization voltage of the Li||Cu cells in PLE only slightly increased and remained stable after increasing the current density. This indicates that the Li^+ transport kinetics has significantly enhanced, attributed to its excellent SEI film performance. In order to analyze the lithium deposition/stripping characteristics during long cycling, we performed Li||Li symmetrical battery tests as

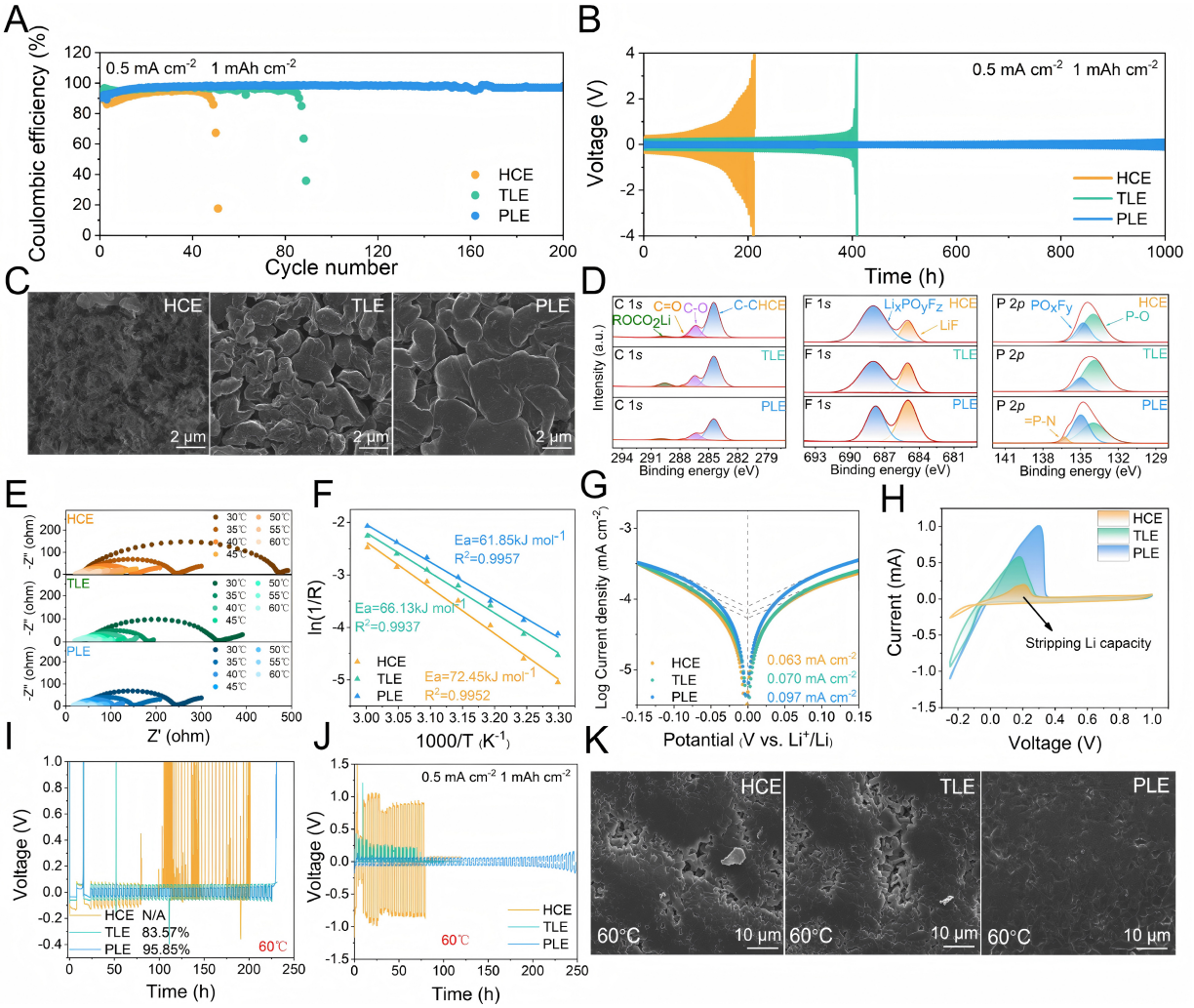

Figure 4. Morphologies and SEI compositions of the cycled Li metal anodes. (A) Coulombic efficiency of Li||Cu cells in HCE, TLE and PLE electrolytes. (B) Voltage-time profiles of Li||Li cells in HCE, TLE and PLE electrolytes. (C) SEM images of deposited Li on Cu substrate in Li||Cu cells with different electrolytes: HCE, TLE and PLE. (D) XPS analysis of C 1s, F 1s, and P 2p of Li metal anodes after 50 cycles in HCE, TLE and PLE electrolytes. (E) Nyquist plots of anode with HCE, TLE and PLE electrolytes. (F) Kinetics energy barrier of Li^+ desolvation by Arrhenius analysis. (G) Tafel plots derived from CV for Li||Li cells with different electrolytes. (H) Cyclic voltammetry profiles for Li||Cu cells at a scan rate of 1 mV s^{-1}. (I) Coulombic efficiency of Li||Cu cells in HCE, TLE and PLE electrolytes at 60 °C tested by modified Aurbach's measurement. (J) Voltage-time profiles of Li||Li cells at 60 °C in HCE, TLE and PLE electrolytes. (K) SEM images of deposited Li in Li||NCM811 cells after 50 cycles at 60 °C in HCE, TLE and PLE electrolytes.

shown in Figure 4B. During the initial cycling, the polarization voltage of the HCE gradually increases and a short circuit occurs after more than 200 h. This may be attributed to interfacial layer thickening and pronounced inhomogeneity during Li plating/stripping, which trigger severe dendrite growth and accumulation of inactive Li, in line with the observed low CE. Although the addition of a diluent enabled modest performance gains for TLE over HCE, the former still failed after 400 h owing to inadequate SEI formation. In stark contrast, PLE exhibited negligible polarization rise and sustained stable cycling for over 1,000 h. The combination of high CE and prolonged reversible Li cycling unambiguously attests to the superior performance of the PLE electrolyte. In addition, we conducted Li||Li cycling tests under different current densities. The capacity for each cycle was 1 mAh·cm^{-2}, and the current density gradually increased from 1 to 4 mA·cm^{-2}. As shown in Supplementary Figure 11, at all current densities, the overpotential of PLE was lower than that of HCE and TLE. Notably, when the current density exceeded 3 mA cm^{-2}, both HCE and TLE exhibited short-circuit phenomena.

To record intuitive morphological features of deposited lithium layers, *in situ* Li||Cu cells were fabricated. Optical microscopy was employed to monitor the Li||Cu cells during galvanostatic discharge at 2 mA cm^{-2} [Supplementary Figure 12]. The HCE electrolyte, owing to its poor interfacial compatibility, gave rise to nonuniform nucleation at the initial deposition stage, which subsequently induced severe tip effects. Within 1 h of deposition, the Li dendrites underwent explosive proliferation. In comparison, TLE produced a nonuniform Li deposition morphology after 1 h of discharge. In contrast, PLE exhibits stable lithium deposition kinetics with uniform nucleation and dense growth. SEM observation of Li deposits on Cu substrates was performed after 50 cycles in Li||Cu cells [Figure 4C]. In HCE and TLE cells, the deposited Li layer exhibited a porous structure riddled with cracks. In contrast, the Li deposited in PLE exhibited a comparatively smooth, dense and flat morphology, which led to fewer side reactions during cycling. PLE electrolytes generate stable SEI films and compact lithium plating layers. Such superior performances stem from its distinctive solvation framework driven by intense dipole-dipole interactions. Comprehensive analysis of *in-situ* and *ex-situ* lithium deposition profiles further verifies that SEI formed in PLE systems achieves higher compactness and uniformity.

The chemical compositions and species distribution of the SEI formed on the LMA after 50 electrochemical cycles were analyzed by XPS, and the corresponding results are exhibited in Figure 4D. The PLE-derived SEI is predominantly composed of inorganic species, with a notably higher proportion of LiF compared to those derived from HCE and TLE. This observation indicates that the defluorination of PFPN during reductive decomposition actively contributes to the construction of a LiF-enriched SEI. In addition to LiF, other inorganic moieties, such as phosphorus-nitrogen species (e.g., =P-N), are also identified, which originate from the deep reduction of PFPN. The synergistic presence of substantial quantities of LiF and =P-N endows the PLE-derived SEI with exceptional mechanical robustness and high ionic conductivity. These characteristics effectively enhance the interfacial stability of the lithium metal anode and suppress undesirable parasitic reactions between the TBP solvent and the LMA, which are otherwise thermodynamically favorable[33,34]. In stark contrast, the SEIs derived from HCE and TLE are characterized by a high content of organic species, as evidenced by significant XPS signatures corresponding to C-C, C-O, C=O, and $ROCO_2Li$ moieties. Such organic-rich interphases are generally less mechanically stable and exhibit lower ionic conductivity, thus providing insufficient protection for the LMA during prolonged cycling[35]. Sputtering XPS [Supplementary Figure 13] results also show that as the sputtering depth increases, the SEI formed in the PLE system has an outer layer mainly composed of organic components, and the inorganic components containing P and N are also significantly enriched in the inner layer, which indicates that the SEI derived from PLE has a gradient structure with a rich organic layer on the outside and an enriched inorganic layer on the inside.

The dipole/pseudo-hydrogen bond synergy between TBP and PFPN leads to distinct solvation structures, which in turn modulate the kinetic and thermodynamic behaviors at the electrolyte-electrode interface[36] Accordingly, the Li^+ desolvation energy barrier serves as a convenient metric to quantify these structural differences [Figure 4E and F]. The desolvation barrier in PLE was measured to be 61.85 kJ mol-1, which is lower than that in TLE (66.13 kJ mol^{-1}) and HCE (72.45 kJ mol^{-1}), indicating that PFPN, acting as a solvation modulator, effectively weakens Li^+-solvent interactions, promotes Li^+ desolvation, and thus improves the kinetic properties. From Tafel analysis [Figure 4G], the interfacial Li^+ transport kinetics were quantitatively evaluated using the exchange current density (I_0). The I_0 of PLE (0.097 mA cm^{-2}) is significantly higher than those of HCE (0.063 mA cm^{-2}) or TLE (0.070 mA cm^{-2}), which indicates faster interfacial Li^+ transport kinetics and the formation of highly conductive SEIs in PLE. As shown in Figure 4H, we conducted additional CV tests on Li||Cu cells. The PLE electrolyte exhibited an enlarged area and discernible redox peaks, suggesting enhanced Li^+ transport and reduced overpotentials. Such a unique solvation environment promotes the formation of SEI layers that favor Li^+ migration, as depicted in Supplementary Figures 14-16.

This interpretation is further supported by EIS analysis of the cells over increasing cycle numbers [Supplementary Table 1]. The elevated R_{SEI} values recorded for HCE and TLE suggest more severe electrolyte degradation during cycling, which gives rise to a corresponding rise in overpotential, while the cathode structure undergoes progressive deterioration from repeated lithiation/delithiation[37]. Conversely, the minimal R_{SEI} of PLE corresponds to a thinner interfacial membrane, thereby favoring lithium-ion dynamics, which indirectly substantiates the merits derived from dipole-dipole interaction. High-temperature performance (60 °C) was evaluated for HCE, TLE and PLE electrolytes. In comparison, short circuiting occurred within the HCE-based Li||Cu cell upon reaching 15 cycles, revealing extensive electrolyte breakdown and dendrite propagation. PLE achieved a CE of 95.85%, outperforming TLE (83.57%) [Figure 4I]. Moreover, the Li||Li symmetric cell with PLE can maintain stable polarization over 250 h [Figure 4J]. After 50 cycles of the Li||NCM811 cells, PLE promoted dense and uniform lithium deposition, whereas HCE and TLE formed porous, whisker-like dendrites [Figure 4K].

Analysis of CEI evolution

In order to verify the integrity of the single-crystal NCM811 morphology cycled in various electrolytes at the voltage range of 2.8-4.4 V, the pristine and cycled electrodes were examined using SEM. After 50 cycles, NCM811 particles demonstrated significant cracking and delamination when tested in HCE and TLE electrolytes [Figure 5A and B]. Conversely, the single-crystal structure of the NCM811 particles in the PLE electrolyte remained intact, a phenomenon that was primarily attributed to the CEI layer promoted by the PLE electrolyte [Figure 5C], which provided additional mechanical support to the cathode, thereby mitigating the propagation of microcracks during cycling. The structural evolution of NCM811 at 60 °C was also investigated using TEM. The NCM811 cycled in PLE exhibits thin and uniform CEI (1.05 nm) [Supplementary Figure 17], indicating PLE constructs robust thin CEI and enhances the interface stability of NCM811 during long-term cycle. In contrast, much thicker CEIs [Supplementary Figure 18] are observed on the NCM811 cycled in TLE (2.21 nm), validating LHCE-TTE is insufficient to construct stable thin CEIs. NCM811 cycled in HCE displays thick CEI (7.93 nm) [Supplementary Figure 19].

The CEI composition after 50 cycles was analyzed by XPS. The PLE-formed CEI featured a high LiF content along with P-O and PO_xF_y species [Figure 5D-F]. These components are mechanically strong and ionically conductive, enabling effective passivation and stabilization of the NCM811 surface. The F 1s spectra further revealed that the LiF proportion in the PLE-derived CEI markedly exceeded that in the HCE- and TLE-derived CEIs, implying that PFPN promotes the generation of LiF-enriched, durable interphase materials. Notably, the CEI derived from PFPN-based LHCE contains more P, N and F elements than TTE-based LHCE CEIs, suggesting that FSI- and PFPN were synergistically formative, contributing to the formation of inorganic-rich CEIs (N-O_x/P-O_x, LiF). These results suggest that PFPN not only reduces electrolyte reactivity, but also promotes the formation of inorganic-rich CEIs by regulating electrolyte degradation. Sputtering XPS results [Supplementary Figure 20] also show that in the CEI formed by PLE, the content of LiF significantly increases with the increase in sputtering depth, and the proportion is much higher than that of HCE and TLE. Moreover, the distribution trends of P-O and LiF show a synchronous enhancement in the depth direction.

Structural instability is a primary cause of rapid capacity fade during extended high-temperature cycling, highlighting the need for studies on the decomposition mechanisms of NCM811 cathodes. Structural degradation is a major contributor to rapid capacity loss under prolonged high-temperature cycling, underscoring the importance of investigating the decomposition behavior of NCM811 cathodes. To track the structural evolution, XRD was used to analyze the NCM811 cathode before and after cycling, with particular attention to its characteristic diffraction peaks. As shown in Figure 5G, peak shifts were observed that indicate variations in lattice parameters. After 50 cycles, the (003) peak exhibited a shift toward lower angles,

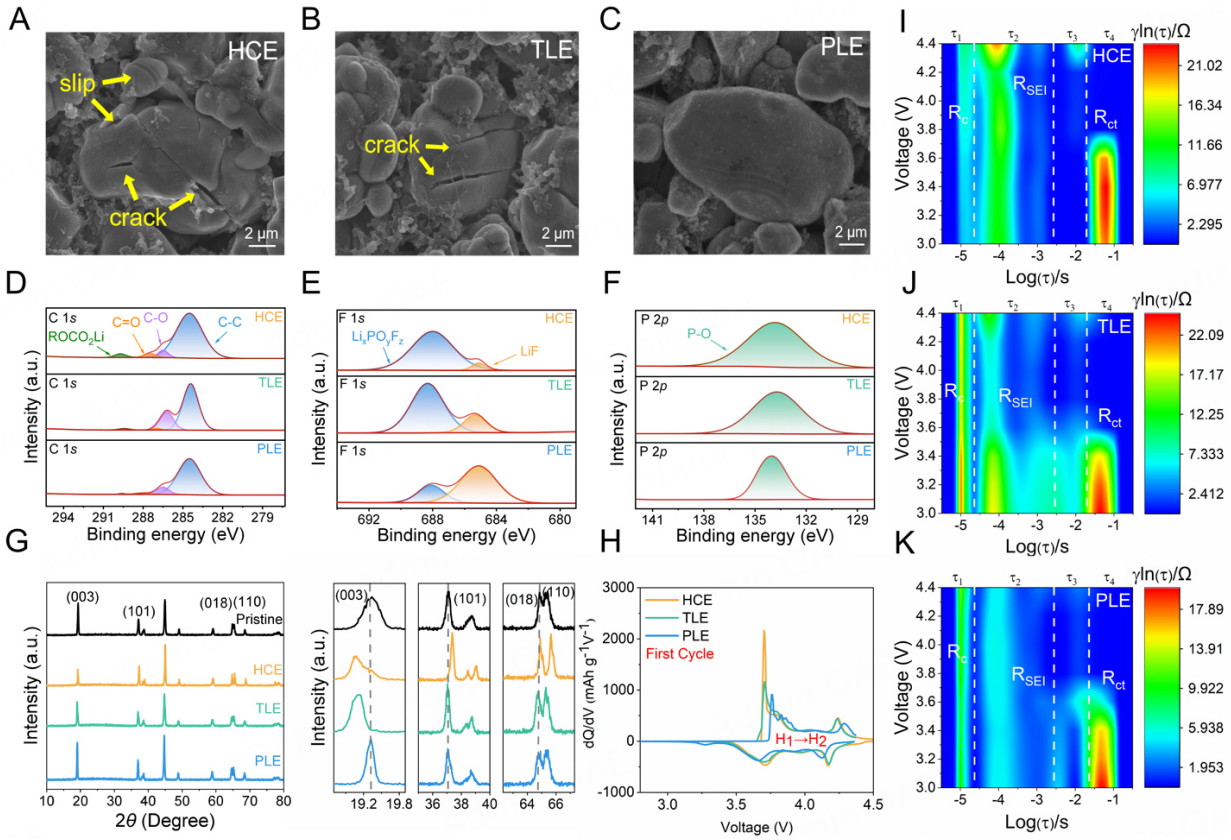

Figure 5. SEM images of morphology of NCM811 cycled in various electrolytes: (A) HCE, (B) TLE and (C) PLE. XPS analysis of (D) C 1s, (E) F 1s, and (F) P 2p of Li||NCM811 cells after 50 cycles in various electrolytes. (G) XRD patterns of NCM811 cathodes in pristine and after 50 cycles in various electrolytes. (H) The dQ/dV curves from the 1st charging and discharging process in HCE, TLE and PLE electrolytes. The initial charge/discharge curve of Li||NCM811 cells was measured at 0.1 C and the corresponding DRT results collected during initial charge/discharge are displayed in (I) HCE, (J) TLE and (K) PLE electrolytes.

indicating a phase transition from H1 to H2 accompanied by an increase in the lattice parameter[38-40]. The (003) XRD peak intensity of NCM811 cathodes cycled in HCE and TLE decreased during the delithiation process, indicating structural degradation, whereas the peak intensity after cycling in PLE remained nearly constant. Phase transformation of the cathode material represents a major factor contributing to battery performance decay[41-43], as evidenced by the dQ/dV analysis presented in Figure 5H. Upon delithiation, the H1 → H2 transition occurs, giving rise to sudden alterations in lattice anisotropy, nonuniform internal stress distribution, and consequent grain-boundary cracking[44]. Furthermore, dQ/dV profiles recorded after 10 and 100 cycles in different electrolytes were systematically compared [Supplementary Figures 21 and 22]. After 100 cycles, the characteristic H1 → H2 peaks for HCE and TLE had almost disappeared, indicating irreversible degradation of the layered cathode structure, which likely accounts for the capacity loss. By contrast, owing to its unique solvation structure based on intermolecular dipole-dipole interactions, the PLE system maintains minimal lattice changes and reversible phase transitions, thus exhibiting excellent cycling stability[45].

To gain deeper insight into the dynamic evolution of Li^+ transport kinetics during the initial charging stage, *in-situ* EIS combined with distribution of relaxation time (DRT) was performed on Li||NCM811 cells throughout the first charge-discharge process. The resulting Nyquist plots for all investigated electrolytes exhibit two distinct characteristic regions: a depressed semicircle in the high-frequency domain, which corresponds to Li^+ diffusion resistance through the SEI (R_{SEI}), and a low-frequency feature attributed to the charge transfer resistance (R_{ct}) at the electrode-electrolyte interface. Notably, as shown in Figure 5I-K and

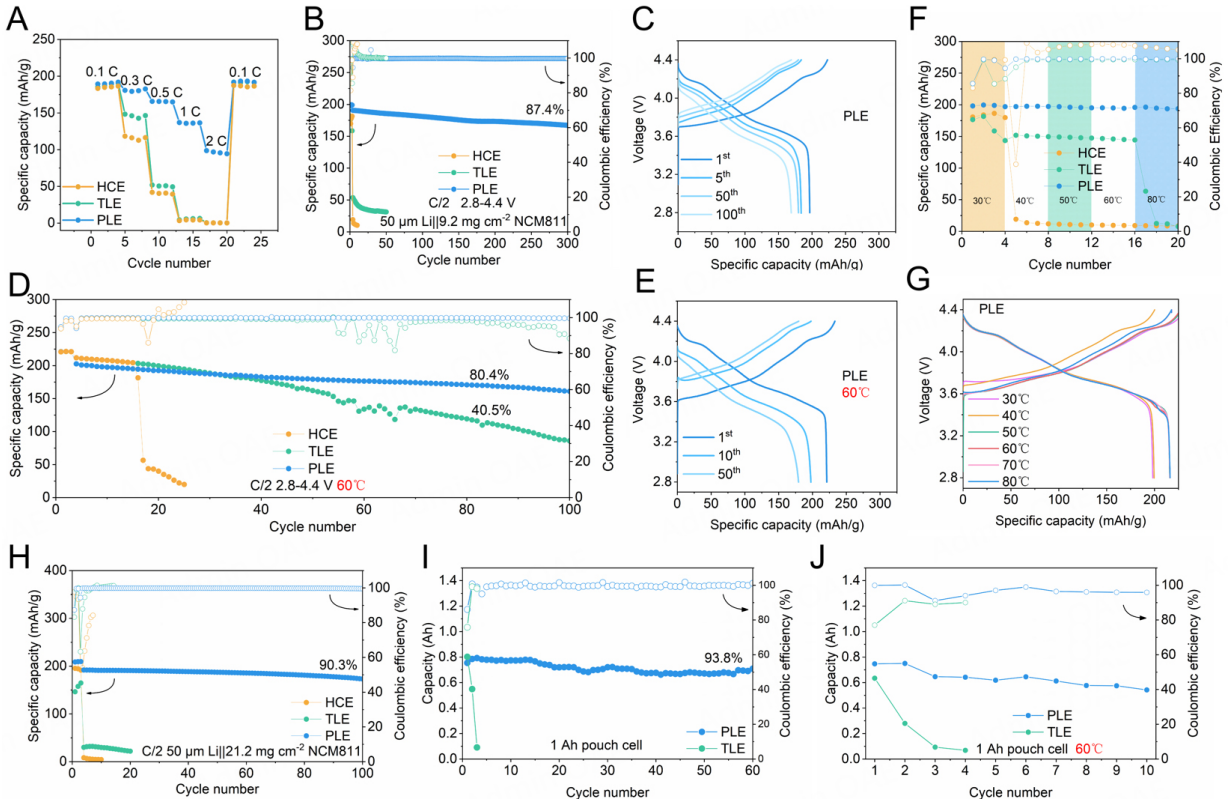

Figure 6. Electrochemical properties. (A) Rate capability of Li||NCM811 cells with HCE, TLE and PLE electrolytes. (B) Cycling performance of Li (50 μm) || NCM811 (9.2 mg cm^{-2}) cells with HCE, TLE and PLE electrolytes at 30 °C. (C) Charge/discharge curves of a Li||NCM811 cell with PLE electrolyte at 30 °C. (D) Cycling performance of the Li (50 μm)||NCM811 (9.2 mg cm^{-2}) cells with HCE, TLE and PLE electrolytes at 60 °C and (E) Charge/discharge curves. (F) Temperature-controlled cycling performance of the Li (50 μm) || NCM811 (9.2 mg cm^{-2}) cells and (G) Corresponding charge/discharge curves. (H) Cycling performance of the Li (50 μm) || NCM811 (21.2 mg cm^{-2}) cells with HCE, TLE and PLE electrolytes at 30 °C. (I) Cycling performance of 1 Ah Li||NCM811 pouch cell using PLE under a 3-4.3 V operating voltage window at 30 °C. (J) Cycling performance of 1 Ah Li||NCM811 pouch cell at 60 °C.

Supplementary Figures 23-25, it can be seen that throughout the charging and discharging process, both R_{SEI} and R_{ct} for the PLE are always lower than for the HCE and TLE. This suggests that the synergistic intermolecular interactions effectively lower the kinetic barrier for Li^+ desolvation, promoting its subsequent intercalation into NCM811.

Electrochemical properties

The electrochemical performance of HCE, TLE, and PLE was compared at elevated temperatures [Figure 6]. The PLE electrolyte cells exhibited faster charge transfer kinetics due to the inorganic-rich interfacial layer resulting from strong dipole-dipole interactions. In the rate capability test [Figure 6A], the batteries using the PLE electrolyte had specific discharge capacities of 136.9 and 101.2 mAh g^{-1} at 1C and 2C, respectively. Li||NCM811 full cells consisting of NCM811 cathodes (9.2 mg cm^{-2}) and thin Li anodes (50 μm) were used to evaluate the performance of PLE in practical LMBs at 30 °C and corresponding charge/discharge curves are shown in Figure 6B and C. After three cycles of activation at C/10 current, the discharge capacities of HCE, TLE and PLE at C/2 current density were 169, 176, and 196 mAh g^{-1}, respectively. The CEs of the first cycle of HCE, TLE and PLE were 81.3%, 85.6% and 88.2%, respectively. The improved discharge capacity and CE stem from enhanced Li^+ transport kinetics and superior compatibility with the LMA. Notably, HCE and TLE became nearly inoperative after merely 10 cycles [Supplementary Figures 26 and 27], whereas PLE sustained over 80% capacity retention after 300 cycles.

At elevated temperatures, the intrinsic instability of the SEI accelerates Li metal degradation and intensifies parasitic reactions between the LMA and the electrolyte[46]. The limited cyclability of LMAs at 60 °C is substantially enhanced by PLE. The initial discharge capacity of Li||NCM811 batteries significantly increases to 221.2 mAh g^{-1} and the batteries still retain 80.4% of the initial capacity after 100 cycles [Figure 6D and E], which demonstrates that the PLE-derived SEI/CEI has excellent high temperature resistance. It has been demonstrated that the accelerated lithium-ion kinetics caused by elevated temperatures can result in enhanced cycling performance for Li||NCM811 cells, particularly when HCE and TLE are employed[47]. However, it should be noted that HCE is only able to cycle normally for a maximum of 10 cycles, while TLE exhibits rapid capacity decay and diminished capacity retention (40.5%) after 100 cycles [Supplementary Figures 28 and 29]. Additionally, wide-temperature testing [Figure 6F and G] demonstrates that Li||NCM811 batteries paired with PLE electrolyte exhibit stable polarization voltage and minimal capacity decay across the 30-80 °C range. This indicates that the mechanism by which PFPN enables rapid desolvation of Li^+, namely by suppressing TBP's binding of Li^+ through a synergistic dipole/pseudo-hydrogen bond interaction, operates over a wide range of temperatures and ensures the battery's cycling performance under high-temperature operating conditions. Furthermore, when paired with a highly loaded LFP electrode (12.3 mg cm^{-2}), the HCE demonstrated an inability to cycle, and the TLE exhibited capacity decay after a mere 20 cycles. Conversely, the PLE exhibited minimal capacity decay (retention rate of 97.5%) after 200 cycles, and the same satisfactory cycling performance was observed at 60 °C [Supplementary Figures 30 and 31]. The excellent electrochemical behavior of PLE not only confirms the stability of the electrolyte-electrode interface but also demonstrates enhanced interfacial compatibility for phosphate esters.

The cycling performance was further evaluated under more stringent conditions using 50 μm Li foil and a higher cathode loading of 21.2 mg cm^{-2}. PLE enabled a high discharge capacity [Figure 6H]. The high oxidation potential of the PLE contributes to the battery's high discharge capacity, with the initial cycle capacity recorded at 208.7 mAh g^{-1}. Notably, 90.3% of the initial capacity is retained after 100 cycles at 0.5C, underscoring the battery's durability. In contrast, HCE and TLE were unable to stabilize the high-loading cathode electrode to the extent that they failed to operate properly after activation. Furthermore, the high-load cathode system of PLE exhibits superior cycling performance compared to the previously reported literature on phosphate ester systems, as shown in Supplementary Table 2. To assess the practical performance of the battery, as shown in Figure 6I and Supplementary Table 3, the Li||NCM811 pouch cell consists of a high-loading NCM811 cathode (26.48 mg cm^{-2} per side, dual-sided coating on Al current collector) paired with a 50 μm lithium metal anode (single-sided). With an electrolyte-to-capacity (E/C) ratio of 1.98 g Ah^{-1} and negative-to-positive (N/P) capacity ratio of 1.09, the cell delivers 1 Ah discharge capacity. The calculated energy density, based on practical discharge energy and measured cell mass, achieves 302 Wh kg^{-1}. With the PLE electrolyte, the cell retains 93.8% capacity after 60 cycles under a 3-4.3 V voltage window at 30 °C. In sharp contrast, with TLE electrolytes the pouch cell showed poor electrochemical performance due to the inferior anode and cathode stability. Notably, even at an elevated temperature of 60 °C, the Ah-level PLE pouch cell successfully completed 10 stable cycles without sudden failure, demonstrating its promising potential for high-temperature practical applications [Figure 6J]. The PLE electrolyte exhibits exceptional thermal stability and high ionic conductivity. Consequently, the PLE electrolyte demonstrates balanced electrochemical performance at both 30 °C and elevated temperatures.

Safety testing

Safety is a primary concern in battery operation, particularly at high temperatures where thermal runaway becomes more likely[48]. The thermal stability of PLE was therefore characterized by DSC. Fully charged NCM811 (4.4 V) was mixed with TLE and PLE at a weight-to-volume ratio of 1:1.2. As shown in Figure 7A,

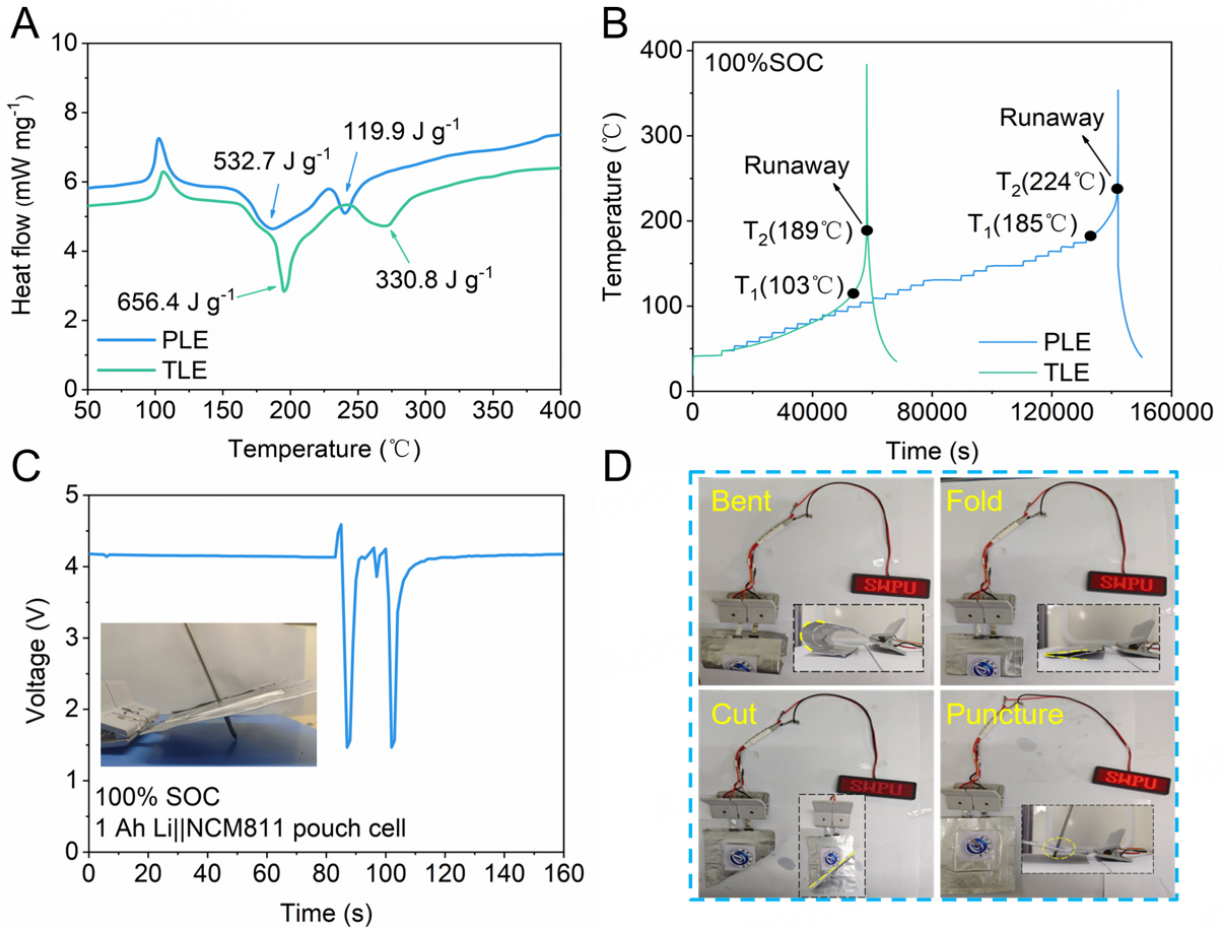

Figure 7. Safety testing of the electrolytes. (A) DSC curves of fully charged NCM811 (4.4 V) mixed with TLE or PLE electrolytes at a weight to volume ratio of 1:1.2 (B) Temperature profiles of 1 Ah Li||NCM811 pouch cells during the ARC tests in TLE and PLE electrolyte. (C) Puncture test of 1 Ah Li||NCM811 pouch cell. (D) Lighting experiments of Li||NCM811 pouch cell under bent, folded, cut and punctured conditions.

the endothermic peak at approximately 100 °C is attributed to TTE volatilization. However, the total heat release from PLE/NCM811 (ΔH = 652.6 J g^{-1}) was lower than that from TLE/NCM811 (ΔH = 987.2 J g^{-1}). The thermal safety of the battery is assessed through the measurement of three characteristic temperatures during testing: T_1, defined as the critical thermal safety threshold; T_2, the onset temperature of thermal runaway; and T_3, the peak temperature attained by the cell[49]. Among these, T_2 serves as the most pivotal parameter in thermal runaway evaluation. Reaching T_2 initiates a cascade of uncontrollable exothermic reactions; the considerable heat released subsequently drives the battery temperature to climb further, eventually culminating in combustion and fire. Consequently, for high-energy-density LMBs, a higher T_2 value signifies enhanced safety and diminished vulnerability to thermal runaway events[50]. In addition, T_3 governs the ultimate severity of the runaway. A combination of elevated T_1 and T_2 readings with a depressed T_3 is indicative of superior overall thermal safety for the battery. ARC measurements were carried out on 1 Ah pouch cells with TLE and PLE to further explore the thermal runaway behavior [Figure 7B]. The cells were tested at a 100% SOC. THE TLE-based pouch cell demonstrates lower onset and runaway temperatures (T_1 = 103 °C, T_2 = 189 °C), whereas the T_1 and T_2 values for PLE-based cell reach 185 and 224 °C, respectively. While both types of pouch cell eventually ignite, the PLE-based cell exhibits a higher thermal runaway temperature and a lower T_3 compared to the TLE-based cell, which indicates that PLE can delay the onset of thermal runaway and reduce the severity of the exothermic reaction, thereby enhancing the overall safety margin under abusive conditions. Such improved safety performance is realized via a special competitive solvation structure constructed with long-chain phosphate ester solvents [Supplementary Table 4].

In practice, sudden external stresses may cause damage, failure, or even thermal runaway, thereby making mechanical abuse testing a means of assessing the safety of batteries[51]. A puncture test of a 1 Ah Li||NCM811 pouch cell with 100% SOC was performed using PLE electrolyte, and the voltage change of the pouch cell during the puncture process was recorded in Figure 7C. Although a sharp voltage drop occurs at the time of puncture, the voltage begins to recover within 10 s, and the initial voltage is restored within the next 50 s. This indicates that the pouch cell based on PLE electrolyte has excellent rapid voltage recovery and high safety, which is attributed to the rapid thermal passivation of phosphate esters at the short-circuit point induced by Joule heating. TBP and PFPN undergo thermal crosslinking/carbonization, synergistically forming a high-resistance physical barrier that blocks the electronic pathway and allows voltage recovery[52]. Meanwhile, the PLE pouch cell has been demonstrated to be capable of powering light-emitting diodes, whilst also exhibiting excellent safety characteristics under mechanical abuse conditions. It also demonstrates excellent safety characteristics under photomechanical stress, such as bending, folding, cutting, and puncturing [Figure 7D], thereby demonstrating the inherent safety of long carbon chain phosphate esters-based pouch batteries.

CONCLUSIONS

In summary, we have demonstrated a rationally designed flame-retardant phosphate-based localized high-concentration electrolyte (PLE) by introducing ethoxylated (pentafluoro)cyclotriphosphazene (PFPN) as a functional diluent. Unlike conventional inert diluents such as TTE, PFPN actively participates in modulating the Li^+ solvation structure through synergistic dipole/pseudo-hydrogen bond interactions. This dual-interaction mechanism effectively weakens Li^+-TBP coordination, promotes anion-rich solvation sheaths, and reduces the desolvation energy barrier, thereby significantly enhancing Li^+ transport kinetics. Moreover, the low LUMO energy level of PFPN enables its preferential reduction on the lithium anode, contributing to the formation of a robust, inorganic-rich SEI composed of LiF and =P-N species, which effectively suppresses parasitic reactions and dendrite growth even at elevated temperatures. On the cathode side, PFPN helps to form a stable, conductive CEI that protects the NCM811 structure over extended cycling. Consequently, PLE enables Li||NCM811 cells to achieve excellent rate capability and prolonged cycling stability at 60 °C. More importantly, Ah-level pouch cells employing PLE demonstrate exceptional safety, withstanding nail penetration at 100% SOC without ignition. This work establishes a new design paradigm for high-performance phosphate electrolytes based on dipole/pseudo-hydrogen bond synergy, offering a promising pathway toward safe and stable high-temperature LMBs.

DECLARATIONS

Authors' contributions

Writing-original draft, visualization, methodology, investigation, data curation, conceptualization: Tao, C.
Software: Han, Z.
Investigation: Shen, Y.; He, Y.; Wang, Y.; Li, G.; Zhao, B.
Supervision, resources: Wang, M.
Writing-review & editing, validation: Zaiser, M.
Writing-review & editing, supervision, resources, conceptualization: Li, X.

Availability of data and materials

The raw data supporting the findings of this study are available within this Article and its Supplementary Materials. Further data are available from the corresponding authors upon request.

AI and AI-assisted tools statement

During the preparation of this manuscript, the AI tool Deepseek (V4-Pro, released 2026-8-14) was used solely for language editing. The tool did not influence the study design, data collection, analysis, interpretation, or the scientific content of the work. All authors take full responsibility for the accuracy, integrity, and final content of the manuscript.

Financial support and sponsorship

This work was supported by the National Major Science and Technology Project-Oil & Gas Major Project (2025ZD1402003).

Conflicts of interest

All authors declared that there are no conflicts of interest.

Ethical approval and consent to participate

Not applicable.

Consent for publication

Not applicable.

Supplementary Materials

Supplementary Materials

REFERENCES

1. Chen, S.; Deng, Z.; Li, J.; et al. Tuning reaction kinetics of fluorinated molecules to construct robust solid electrolyte interphases on SiO_x anode. *Angew. Chem. Int. Ed.* **2024**, *64*, e202413927. DOI
2. Cheng, H.; Ma, Z.; Kumar, P.; et al. Non-flammable electrolyte mediated by solvation chemistry toward high-voltage lithium-ion batteries. *ACS. Energy. Lett.* **2024**, *9*, 1604-16. DOI
3. Chen, W.; Sun, C. Recent advances in high temperature solid oxide electrolytic cells. *Energy. Mater.* **2025**, *5*, 500045. DOI
4. Deng, Z.; Jia, Y.; Deng, Y.; et al. Coordination structure regulation in non-flammable electrolyte enabling high voltage lithium electrochemistry. *J. Energy. Chem.* **2024**, *96*, 282-90. DOI
5. Qiao, R.; Zhao, Y.; Zhou, S.; et al. Non-fluorinated electrolytes with micelle-like solvation for ultra-high-energy-density lithium metal batteries. *Chem* **2025**, *11*, 102306. DOI
6. Fang, M.; Yue, X.; Dong, Y.; Chen, Y.; Liang, Z. A temperature-dependent solvating electrolyte for wide-temperature and fast-charging lithium metal batteries. *Joule* **2024**, *8*, 91-103. DOI
7. Feng, Y.; Zhou, L.; Ma, H.; et al. Challenges and advances in wide-temperature rechargeable lithium batteries. *Energy. Environ. Sci.* **2022**, *15*, 1711-59. DOI
8. Hai, F.; Yi, Y.; Xiao, Z.; et al. A low-cost, fluorine-free localized highly concentrated electrolyte toward ultra-high loading lithium metal batteries. *Adv. Energy. Mater.* **2024**, *14*, 2304253. DOI
9. He, R.; Zhang, Q.; Hu, Y.; et al. Partially sacrificial hybrid diluent regulated electrolytes boosting wide-temperature Li metal batteries. *Energy. Storage. Mater.* **2024**, *73*, 103836. DOI
10. Kautz, D. J.; Cao, X.; Gao, P.; et al. Designing electrolytes with controlled solvation structure for fast-charging lithium-ion batteries. *Adv. Energy. Mater.* **2023**, *13*, 2301199. DOI
11. Kim, S.; Park, G.; Lee, S. J.; et al. Lithium-metal batteries: from fundamental research to industrialization. *Adv. Mater.* **2023**, *35*, 2206625. DOI
12. Lee, K.; Kwon, S.; Kim, J.; et al. Fluorinated cyclic ether diluent for high-voltage lithium metal batteries. *ACS. Energy. Lett.* **2024**, *9*, 2201-11. DOI
13. Lee, S.; Su, L.; Mesnier, A.; Cui, Z.; Manthiram, A. Cracking vs. surface reactivity in high-nickel cathodes for lithium-ion batteries. *Joule* **2023**, *7*, 2430-44. DOI
14. Li, M.; Chen, Y.; Wu, S.; et al. Tuning solvation structure via inductive and steric hindrance effects for high-voltage $LiCoO_2$ batteries. *Angew. Chem. Int. Ed.* **2025**, *64*, e202514299. DOI
15. Li, P. C.; Zhang, Z. Q.; Zhao, Z. W.; et al. Dipole moment influences the reversibility and corrosion of lithium metal anodes. *Adv. Mater.* **2024**, *36*, 2406359. DOI
16. Lin, Y.; Yang, Z.; Zhang, X.; et al. Activating ultra-low temperature Li-metal batteries by tetrahydrofuran-based localized saturated electrolyte. *Energy. Storage. Mater.* **2023**, *58*, 184-94. DOI
17. Liu, M.; Zeng, Z.; Gu, C.; et al. Ethylene carbonate regulated solvation of triethyl phosphate to enable high-conductivity, nonflammable, and graphite compatible electrolyte. *ACS. Energy. Lett.* **2023**, *9*, 136-44. DOI

18. Liu, M.; Zeng, Z.; Wu, Y.; et al. Reviewing recent progress of liquid electrolyte chemistry for mitigating thermal runaway in lithium-ion batteries. *Energy. Storage. Mater.* **2024**, *65*, 103133. DOI
19. Liu, Q.; Liu, Y.; Chen, Z.; et al. An inorganic-dominate molecular diluent enables safe localized high concentration electrolyte for high-voltage lithium-metal batteries. *Adv. Funct. Mater.* **2022**, *33*, 2209725. DOI
20. Liu, X.; Li, S.; Yuan, C.; et al. Probing the heterogeneous nature of LiF in solid-electrolyte interphases. *Nature* **2025**, *646*, 102-7. DOI
21. Liu, Y.; Zeng, T.; Li, G.; et al. The surface double-coupling on single-crystal $LiNi_{0.8}Co_{0.1}Mn_{0.1}O_2$ for inhibiting the formation of intragranular cracks and oxygen vacancies. *Energy. Storage. Mater.* **2022**, *52*, 534-46. DOI
22. Luo, C.; Liu, Q.; Wang, X.; et al. Synergistic-effect of diluent to reinforce anion-solvation-derived interfacial chemistry for 4.5 V-class Li||$LiCoO_2$ batteries. *Nano. Energy.* **2023**, *109*, 108323. DOI
23. Luo, H.; Ji, X.; Lin, H.; et al. Establishing the field-flow competition model to decipher the nonmonotonic interfacial Li^+ dynamic process for stabilizing the high-voltage cathode-electrolyte interface. *J. Am. Chem. Soc.* **2025**, *147*, 38128-40. DOI
24. Ma, P.; Kumar, R.; Wang, K.; Amanchukwu, C. V. Active learning accelerates electrolyte solvent screening for anode-free lithium metal batteries. *Nat. Commun.* **2025**, *16*, 8396. DOI PubMed PMC
25. Ma, T.; Ni, Y.; Wang, Q.; et al. Optimize lithium deposition at low temperature by weakly solvating power solvent. *Angew. Chem. Int. Ed.* **2022**, *61*, e202207927. DOI
26. Mo, Y.; Liu, G.; Chen, J.; et al. Unraveling the temperature-responsive solvation structure and interfacial chemistry for graphite anodes. *Energy. Environ. Sci.* **2024**, *17*, 227-37. DOI
27. Ni, Z.; Wei, C.; Wang, Z.; et al. Tri-anions regulated solvation structure in intrinsically nonflammable phosphate-based electrolytes for stable lithium metal batteries. *Energy. Storage. Mater.* **2024**, *71*, 103603. DOI
28. Ou, Y.; Hou, W.; Zhu, D.; et al. Molecular design of electrolyte additives for high-voltage fast-charging lithium metal batteries. *Energy. Environ. Sci.* **2025**, *18*, 1464-76. DOI
29. Zeng, Z.; Murugesan, V.; Han, K. S.; et al. Non-flammable electrolytes with high salt-to-solvent ratios for Li-ion and Li-metal batteries. *Nat. Energy.* **2018**, *3*, 674-81. DOI
30. Shi, J.; Nguyen, H.; Chen, Z.; et al. Nanostructured block copolymer single-ion conductors for low-temperature, high-voltage and fast charging lithium-metal batteries. *Energy. Mater.* **2023**, *3*, 300036. DOI
31. Shi, J.; Xu, C.; Lai, J.; et al. An amphiphilic molecule-regulated core-shell-solvation electrolyte for Li-metal batteries at ultra-low temperature. *Angew. Chem. Int. Ed.* **2023**, *62*, e202218151. DOI
32. Shuchi, S. B.; D'acunto, G.; Sayavong, P.; et al. Cryogenic X-ray photoelectron spectroscopy for battery interfaces. *Nature* **2025**, *646*, 850-5. DOI
33. Sun, Q.; Cao, Z.; Ma, Z.; et al. Dipole-dipole interaction induced electrolyte interfacial model to stabilize antimony anode for high-safety lithium-ion batteries. *ACS. Energy. Lett.* **2022**, *7*, 3545-56. DOI
34. Sun, S.; Zhang, X.; Yan, X.; Zheng, Z.; Zhang, Q.; Huang, J. Advances in high-coulombic-efficiency lithium metal anodes under practical conditions in liquid electrolytes. *EES. Batter.* **2025**, *1*, 340-63. DOI
35. Tian, J.; Wang, G.; Zeng, W.; et al. A bimetal strategy for suppressing oxygen release of 4.6 V high-voltage single-crystal high-nickel cathode. *Energy. Storage. Mater.* **2024**, *68*, 103344. DOI
36. Wang, J.; Li, Y.; Tu, W.; et al. Regulating dynamic evolution of interfacial electrolyte configuration via inert cation induced anion anchoring to stabilize lithium-metal anode. *Angew. Chem. Int. Ed.* **2025**, *64*, e202513839. DOI
37. Wang, M.; Lv, S.; Li, M.; et al. A heterogeneous quasi-solid-state hybrid electrolyte constructed from electrospun nanofibers enables robust electrode/electrolyte interfaces for stable lithium metal batteries. *Adv. Fiber. Mater.* **2024**, *6*, 727-38. DOI
38. Wang, X. L.; Li, Y.; Liu, J.; et al. A robust dual-layered solid electrolyte interphase enabled by cation specific adsorption-induced built-in electrostatic field for long-cycling solid-state lithium metal batteries. *Angew. Chem. Int. Ed.* **2025**, *64*, e202421101. DOI
39. Wang, Z.; Chen, C.; Wang, D.; Zhu, Y.; Zhang, B. Stabilizing interfaces in high-temperature NCM811-Li batteries via tuning terminal alkyl chains of ether solvents. *Angew. Chem. Int. Ed.* **2023**, *62*, e202303950. DOI
40. Wang, Z.; Wang, Y.; Li, B.; et al. Non-flammable ester electrolyte with boosted stability against Li for high-performance Li metal batteries. *Angew. Chem. Int. Ed.* **2022**, *61*, e202206682. DOI PubMed PMC
41. Wen, Z.; Fang, W.; Wang, F.; et al. Dual-salt electrolyte additive enables high moisture tolerance and favorable electric double layer for lithium metal battery. *Angew. Chem. Int. Ed.* **2024**, *63*, e202314876. DOI
42. Wu, D.; Zhu, C.; Wang, H.; et al. Mechanically and thermally stable cathode electrolyte interphase enables high-temperature, high-voltage Li||$LiCoO_2$ batteries. *Angew. Chem. Int. Ed.* **2024**, *63*, e202315608. DOI
43. Xiang, S.; Zhu, L.; Fu, L.; et al. Cryogenic and in situ characterization techniques for electrode interphase analysis. *eScience* **2025**, *5*, 100291. DOI

44. Xu, D.; Yang, C.; Yang, A.; et al. Nonflammable electrolyte with weak-solvation structure for stable NCM811 cathode under high temperature. *J. Energy. Chem.* **2025**, *104*, 111-7. DOI
45. Xu, J.; Zhang, J.; Pollard, T. P.; et al. Electrolyte design for Li-ion batteries under extreme operating conditions. *Nature* **2023**, *614*, 694-700. DOI
46. Xu, Z.; Zhang, X.; Yang, J.; Cui, X.; Nuli, Y.; Wang, J. High-voltage and intrinsically safe electrolytes for Li metal batteries. *Nat. Commun.* **2024**, *15*, 9856. DOI PubMed PMC
47. Zhao, H.; Hu, S.; Fan, Y.; et al. Significance of electrolyte additive molecule structure in stabilizing interphase in $LiNi_{0.8}Co_{0.1}Mn_{0.1}O_2$/artificial graphite pouch cells at high temperature. *Energy. Storage. Mater.* **2024**, *65*, 103151. DOI
48. Zhang, C.; Gu, S.; Zhang, D.; et al. Nonflammable, localized high-concentration electrolyte towards a high-safety lithium metal battery. *Energy. Storage. Mater.* **2022**, *52*, 355-64. DOI
49. Zheng, Z.; Zhang, X.; Zhan, D.; et al. Elucidating the solvating power of solvents for designing high-performance electrolytes in lithium batteries. *ACS. Energy. Lett.* **2025**, *10*, 4962-82. DOI
50. Zhou, J.; Ma, B.; Wang, Q.; et al. Anion-regulated weakly solvation sulfolane-based electrolyte towards high-voltage lithium metal batteries. *Chem. Eng. J.* **2025**, *504*, 158857. DOI
51. Zou, Y.; Ma, Z.; Liu, G.; et al. Non-flammable electrolyte enables high-voltage and wide-temperature lithium-ion batteries with fast charging. *Angew. Chem. Int. Ed.* **2023**, *62*, e202216189. DOI
52. Li, X.; Li, W.; Chen, L.; et al. Ethoxy (pentafluoro) cyclotriphosphazene (PFPN) as a multi-functional flame retardant electrolyte additive for lithium-ion batteries. *J. Power. Sources.* **2018**, *378*, 707-16. DOI